

---

NEPTUNE\_CFD SIMULATIONS OF DEBORA-PROMOTEUR AND AGATE-PROMOTEUR CASES

---

## Contents

11.1 NEPTUNE_CFD simulations of DEBORA-Promoteur cases . . . . .	<b>175</b>
11.1.1 Simulation Setup . . . . .	175
11.1.2 Results . . . . .	176
11.2 NEPTUNE_CFD simulations of AGATE-Promoteur cases . . . . .	<b>178</b>
11.2.1 Simulation Setup . . . . .	178
11.2.2 Results . . . . .	179
11.3 Regarding CHF Detection in Mixing Vanes Geometry . . . . .	<b>183</b>
11.4 Conclusions . . . . .	<b>185</b>

---

In this Chapter, we conduct NEPTUNE\_CFD simulations of the DEBORA-Promoteur and AGATE-Promoteur experiments. The results are presented as a prospective study of the capacity of the code to handle complex geometries approaching the industrial configuration.

### 11.1 NEPTUNE\_CFD SIMULATIONS OF DEBORA-PROMOTEUR CASES

#### 11.1.1 *Simulation Setup*

Contrary to the DEBORA simulations (Chapter 4), the physics involved in the DEBORA-Promoteur case are intrinsically three-dimensional. Therefore, the problem can not be reduced to 2D-axisymmetric computations. The computational domain is thus a 4m long vertical tube of radius  $R = 9.6$  mm, with base of the mixing blades positioned at the axial height  $z = 0$ . The heated section is translated axially to adapt the simulation for each position of the mixing vanes (23.5  $D_h$  for C4800 and 10  $D_h$  for C5200), giving the following boundary conditions:

- Uniform wall heat flux for  $-3.055 \text{ m} \leq z \leq 0.445 \text{ m}$  (C4800) or  $-3.318 \text{ m} \leq z \leq 0.182 \text{ m}$  (C5200) ;
- Adiabatic wall for remaining wall faces ;
- Uniform outlet pressure ;
- Uniform liquid inlet velocity and temperature.

A mesh sensitivity conducted to use the mesh presented on Figure 11.1 which contains a total of 3 487 267 cells.

We simulated 3 cases per series 48G3P26WA and 52G3P26WA, covering the two MV positions and different outlet quality ( $x_{eq,out}$ ) :

- 48G3P26WATE65 & 52G3P26WATE65 with  $x_{eq,out} \approx 0\%$
- 48G3P26WATE69 & 52G3P26WATE69 with  $x_{eq,out} \approx 5\%$
- 48G3P26WATE75 & 52G3P26WATE75 with  $x_{eq,out} \approx 12.5\%$

**Note :** The computational times was ensured to be long enough to reach time-average convergence of the simulations.

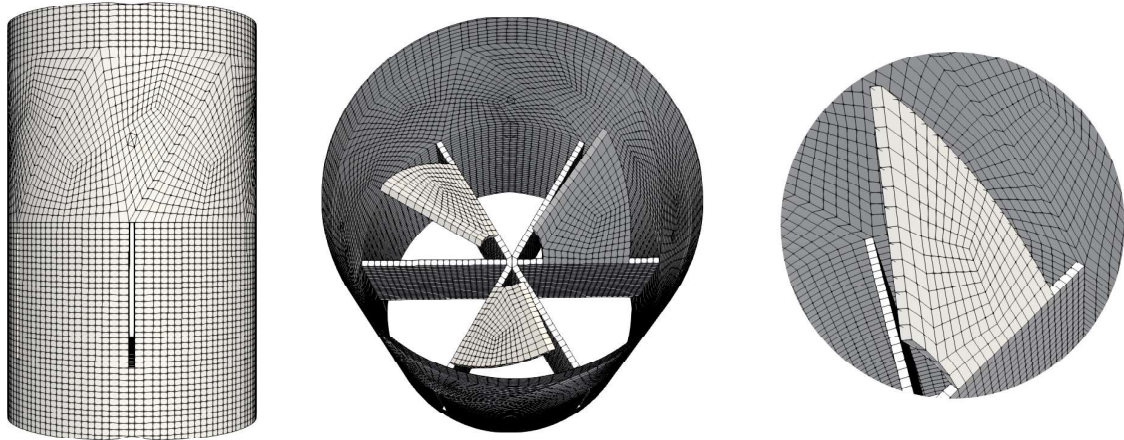


Figure 11.1: Meshing of the mixing vanes region.

Results are compared to the experimental measurements *i. e.* only void fraction for C4800 cases and void fraction, bubble diameter and vapor velocity for C5200 cases.

**Remark :** Following the discussions regarding vapor velocity and bubble diameter estimation for C5200 cases (Chapter 10), comparison with the CFD results will rather be of qualitative nature since we can't ensure the accuracy of the measurements.

### 11.1.2 Results

Results are presented on Figure 11.2.

Quantitatively speaking, it seems that NEPTUNE\_CFD reproduces the effect of vapor accumulation at the center under the pressure gradient generated by the swirl induced by the mixing vanes. The radial position of the core void fraction peak correctly matches the experimental one. The Te65 cases (Figure 11.2a) are reasonably predicted with void fractions values at the center close to the measurements, with the C5200 simulation much closer to the experimental profile. However, Te69 and Te75 cases (Figures 11.2b and 11.2c) are showing much larger discrepancies with the experiments. The core void fraction peak appears largely overestimated for  $T_{L,in} = 69^\circ\text{C}$  with  $\alpha(r/R = 0) \approx 70\%$  and do not change when moving to  $T_{L,in} = 75^\circ\text{C}$  where the void fraction profile rather flattens. Such a behavior strongly differs from the experiments where a large increase in core void fraction when inlet temperature increases. Moreover, the particular shape of 52G3P26WATe75 case where local maximum for  $\alpha$  are observed at  $r/R \approx \pm 0.6$ .

**Remark :** The computed void fraction seems unable to go above 70% in this case, which is in contradiction with the experiments. However, a sensitivity test showed that removing the added mass force (Eq. 2.24) from the interfacial momentum transfer allowed the bulk void fraction to reach 90%.

Regarding C5200 cases, bubble diameter profiles appear coherent with the experimental estimations for Te65 and Te69 cases (Figure 11.2d and 11.2e). In particular, the growth towards the center due to coalescence is fairly reproduced in Te69 case. On the contrary, the very large estimated values for Te75 case ( $D_V \sim 2 \text{ mm}$ ) are completely missed by the simulation (Figure 11.2f).

**Remark :** As discussed in the analysis of the experimental results (Subsection 10.4.1), the flow regime encountered in the 52G3P26W3Te75 case is very likely deviate from a dispersed bubbly flow, explaining the inability of the simulations to reproduce this behavior.

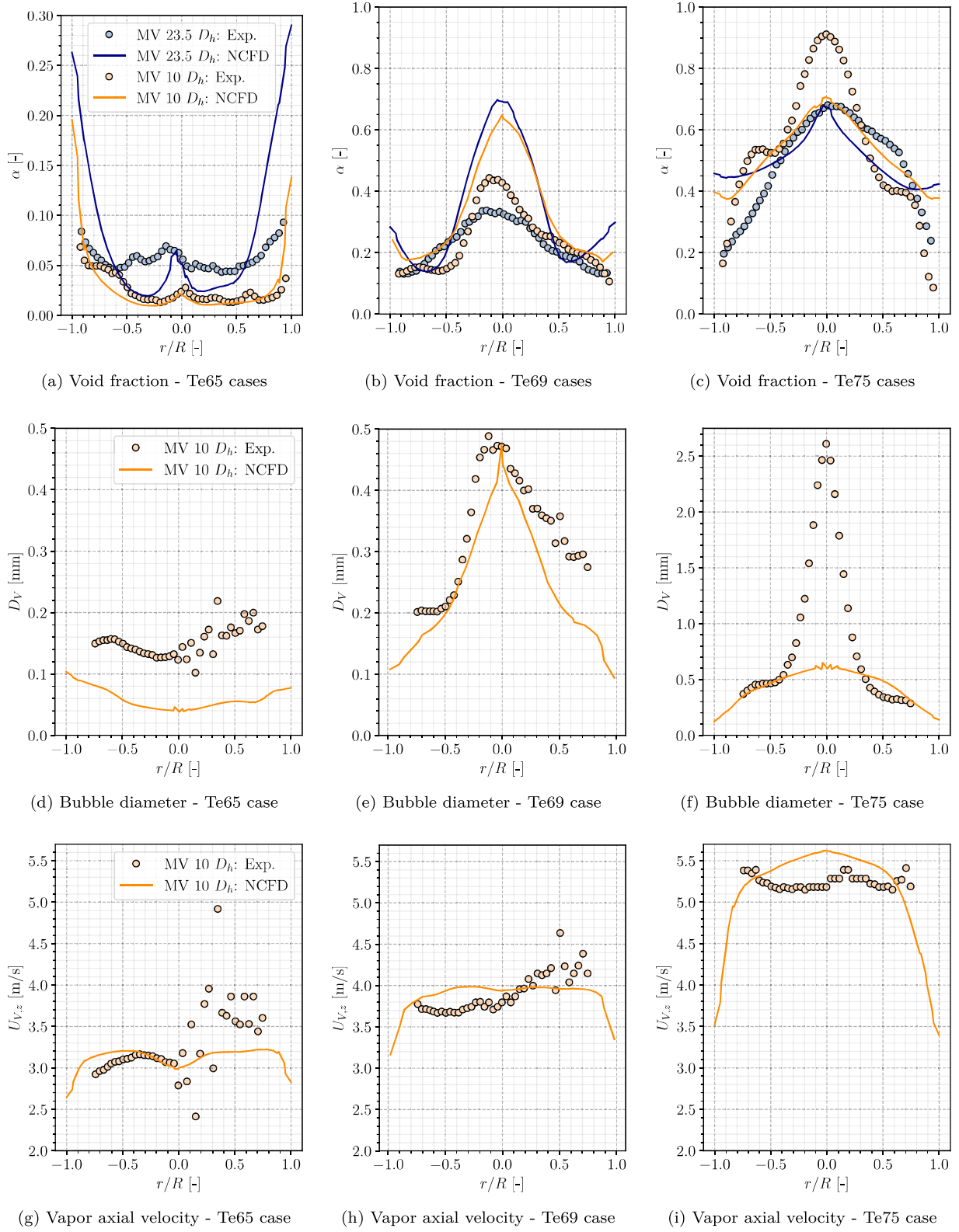


Figure 11.2: NCFD results on the DEBORA-Promoteur cases. MV at  $23.5 D_h$  and  $10 D_h$  respectively correspond to C4800 and C5200 cases.

Finally, the order of magnitude of predicted vapor velocities increases with the inlet temperature (Figures 11.2g, 11.2h, 11.2i) similarly to the experimental estimations.

To further investigate the mixing vanes geometry and understand the large discrepancies on the void fraction profiles (Figures 11.2b and 11.2c), we perform simulations of the single-phase AGATE-Promoteur case in next Section.

## 11.2 NEPTUNE\_CFD SIMULATIONS OF AGATE-PROMOTEUR CASES

### 11.2.1 *Simulation Setup*

Simulations of the AGATE-Promoteur case are done using *code\_saturne* 7.0, the single-phase counterpart of NEPTUNE\_CFD. The computational domain is 0.7 m long (shorter than DEBORA-Promoteur case since we don't need to apply the 3.5m heating) with the mixing blades positioned at  $z = 0$ . Using the same meshing used for the DEBORA-Promoteur cases (Figure 11.1), the total mesh contains 1 905 357 cells.

Two simulations are performed using the turbulence model  $R_{ij} - \varepsilon$  SSG with a smooth wall two-scale turbulent law and with a rough wall turbulent law (average roughness  $\epsilon = 10^{-5}$  m fixed arbitrarily as a sensitivity test) [182].

**Note :** Before comparisons with experiments, we made sure that NEPTUNE\_CFD two-phase solver and *code\_saturne* single-phase solver produced similar results when simulating a single-phase flow using the  $R_{ij} - \varepsilon$  SSG model.

To test the sensitivity to turbulence modeling, we also realize a Large Eddy Simulation (LES) using the LES WALE (Wall-Adapting Local Eddy-Viscosity) model [119]. For this simulation, we use a more refined mesh (Figure 11.3) containing a total of 121 942 848 cells.

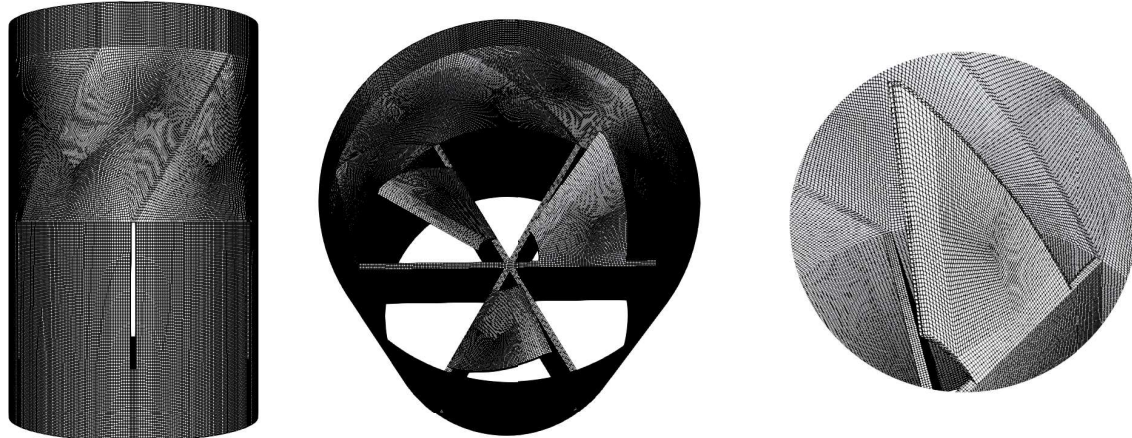


Figure 11.3: Fine meshing of the mixing vanes region for the LES calculation.

In this configuration, we achieve an average wall distance  $y^+ \approx 13$  in the whole domain, which is too large to numerically resolve the boundary layer meaning a wall-law will be used to evaluate the liquid velocity in the wall cell.

**Note :** A stable time-convergence of all the variables is achieved for the LES computation after 10 s of simulated physical time.

Finally, we want to compare the results of the simulations with measurements of the RMS of the velocity fluctuations (Eq. 10.1), meaning that we have to reconstruct those values from the CFD computations. Since we perform Unsteady-RANS (URANS) simulations (using the  $R_{ij} - \varepsilon$  SSG model), fluctuations of the velocity field are both modeled in the components of the Reynolds Stress Tensor and partly simulated

due to the potential time-oscillations of the average velocity field  $\langle \bar{U} \rangle$ . Therefore, the RMS for URANS simulations is computed using the modeled components of the Reynolds Stress Tensor  $R_{ij,mod}$ :

$$RMS_{A,URANS} = \sqrt{R_{zz,mod} + \langle (\tilde{U} \otimes \tilde{U})_{zz} \rangle} \quad (11.1)$$

where  $\tilde{U} = \langle \bar{U} \rangle - \bar{U}$  is the instantaneous difference between the velocity field and its time average *i.e.* the simulated fluctuations of the URANS computation.

Regarding the LES computation, the fluctuations of the velocity field are mainly simulated and are thus only contained in the instantaneous velocity field  $\bar{U}$ . Therefore, they are computed as:

$$RMS_{A,LES} = \sqrt{\langle (\tilde{U} \otimes \tilde{U})_{zz} \rangle} \quad (11.2)$$

The same operation is conducted for the radial RMS, which involves the components  $xx$ ,  $yy$  and  $xy$ .

### 11.2.2 Results

In this section, we discuss results obtained at three different heights :  $0.8 D_h$ ,  $10 D_h$  and  $23 D_h$  downstream the mixing vanes.

#### 11.2.2.1 $0.8 D_h$ After the Mixing Vanes

Figure 11.4 shows the results less than a hydraulic diameter after the mixing vanes.

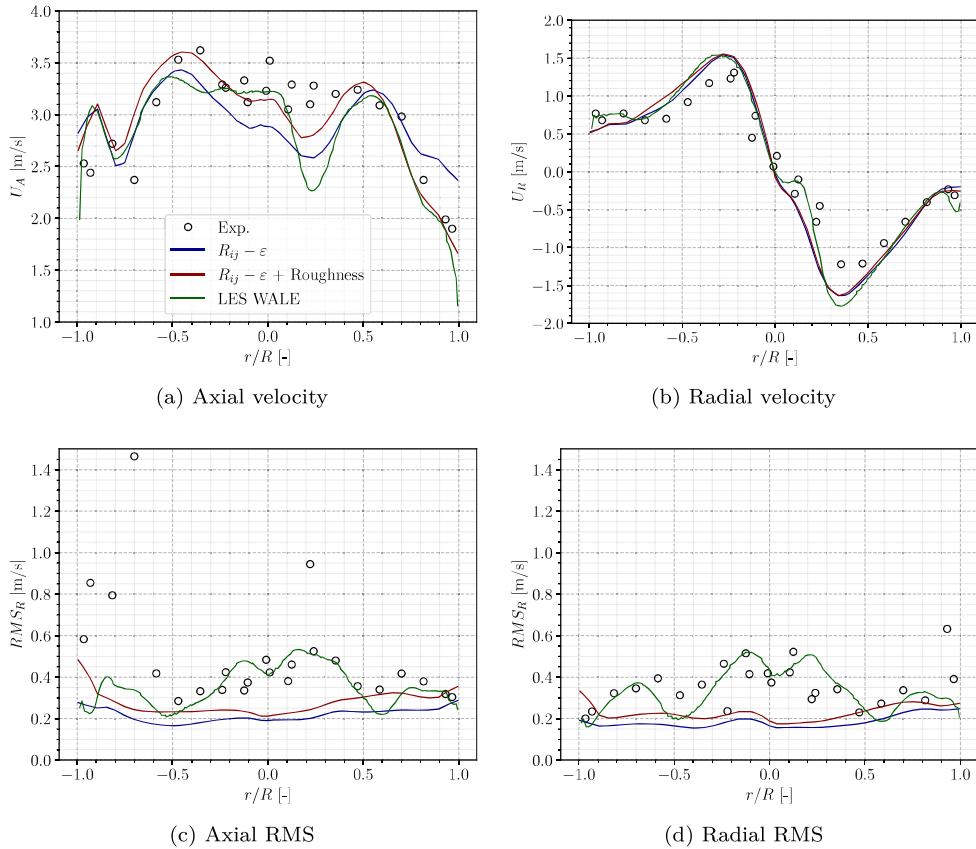


Figure 11.4: Results for  $z = 0.8 D_h$

The three simulations correctly match the experiments for the axial and radial velocities (Figures 11.4a and 11.4b). However, the velocity RMS (Figures 11.4c and 11.4d) are underestimated by the  $R_{ij} - \epsilon$  model, with the rough law use yielding slightly higher values. On the contrary, the LES simulation better reproduce the core velocity fluctuations especially near the center of the pipe.

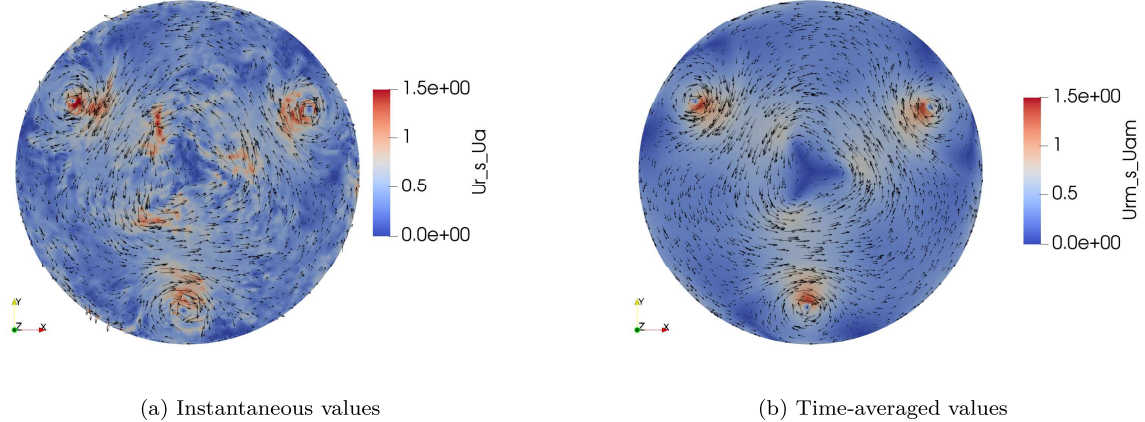


Figure 11.5: Visualization of the radial velocity field and ratio between radial and axial velocity obtained with the LES,  $z = 1 D_h$  downstream the MV.

Figure 11.5 shows the ratio of radial to axial velocity  $1 D_h$  after the vanes for the LES computation.

### 11.2.2.2 $10 D_h$ After the Mixing Vanes

Figure 11.6 shows the results at  $10 D_h$  downstream the mixing vanes, which corresponds to the distance at which two-phase flow measurements of the DEBORA-Promoteur C5200 campaign was conducted (Section 10.2).

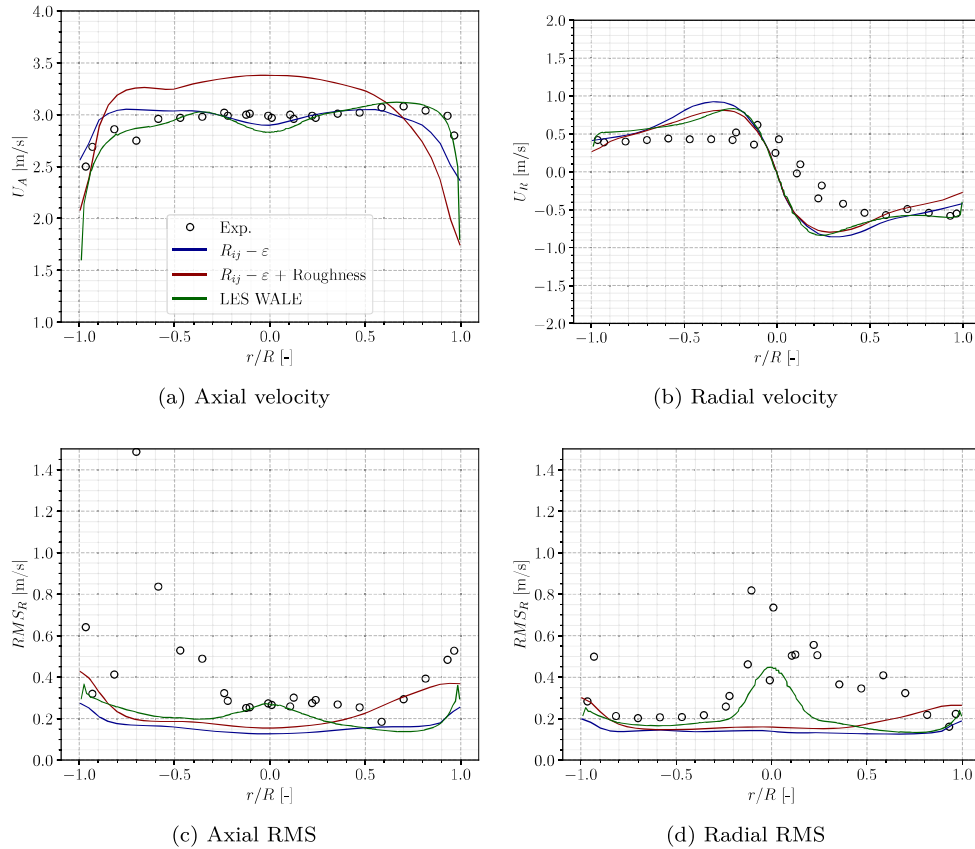


Figure 11.6: Results for  $z = 10.4 D_h$

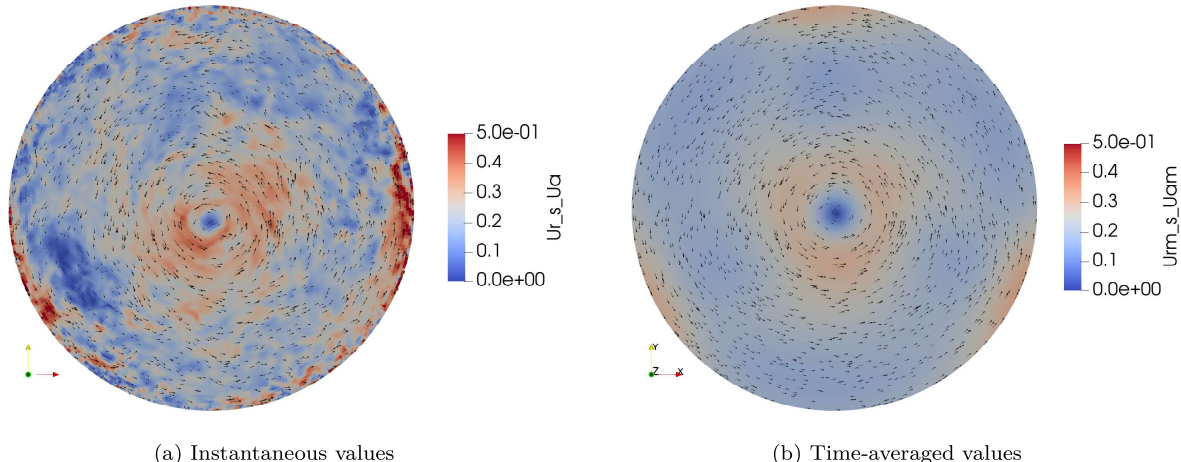


Figure 11.7: Visualization of the radial velocity field and ratio between radial and axial velocity obtained with the LES,  $z = 10 D_h$  downstream the MV.

Going further downstream, we observe that the use of the roughness law start to induce discrepancies on the axial velocity profile while the two other calculations still agree with the measurements (Figure 11.6a). Radial velocity is however equally predicted by the three simulations, with well reproduced wall values but all showing overestimation for  $-0.5 \leq r/R \leq 0.5$  (Figure 11.6b), meaning that a too large bulk rotation of the fluid is predicted.

The velocity RMS are still better predicted by the LES computation (Figures 11.6c and 11.6d) but start to show underpredictions compared to the  $1 D_h$  results. Close to the wall, the three modeling all perform similarly.

Figure 11.7 shows the ratio of radial to axial velocity  $10 D_h$  after the vanes for the LES computation.

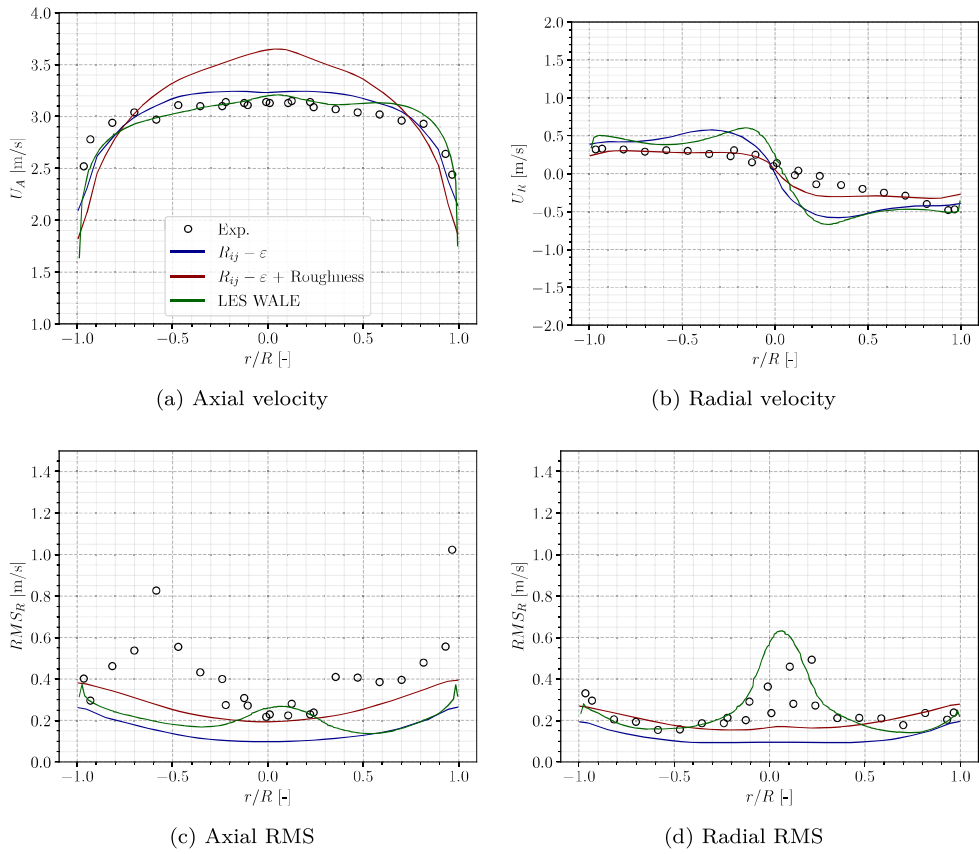
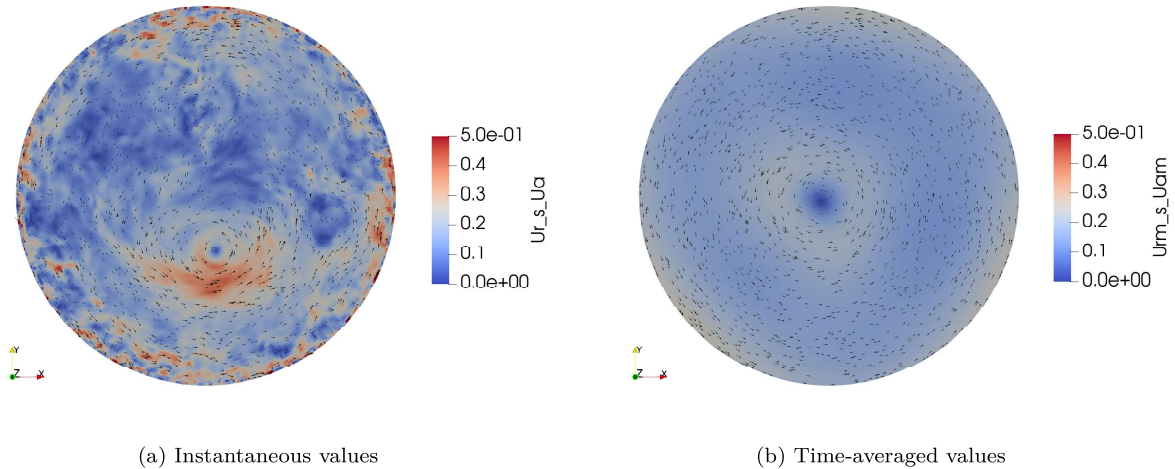
### 11.2.2.3 23 $D_h$ After the Mixing Vanes

Finally, Figure 11.8 present results  $23.5 D_h$  downstream the mixing vanes, which corresponds to the distance at which two-phase flow measurements of the DEBORA-Promoteur C4800 campaign was conducted (Section 10.2).

At this distance, the axial velocity profile has been significantly degraded by using the roughness law (Figure 11.8a) where the other modelings continue to match the measurements. However, the overestimation of the rotation velocity is amplified compared to the  $10 D_h$  results for the smooth wall simulations while adding a roughness term seem to enhance the damping of the swirl induced by the vanes, better reproducing the experimental results (Figure 11.8b).

The axial velocity RMS are now better predicted by the rough wall simulation (Figure 11.8c) while the radial RMS is more accurately reproduced by the LES computation (Figure 11.8d).

Figure 11.9 shows the ratio of radial to axial velocity  $23 D_h$  after the vanes for the LES computation.

Figure 11.8: Results for  $z = 22.9 D_h$ Figure 11.9: Visualization of the radial velocity field and ratio between radial and axial velocity obtained with the LES,  $z = 23 D_h$  downstream the MV.

#### 11.2.2.4 Interpretation Regarding the DEBORA-Promoteur Simulations

Overall, the main characteristic of the single-phase simulation results on the AGATE-Promoteur case is the overestimation of the radial velocity when moving downstream the mixing vanes and reaching the axial positions corresponding to C4800 and C5200 measurements. In terms of hydrodynamics, it means the fluid's rotation is too large, which will result in a stronger pressure gradient between the wall and the center.

Transposing this result to a bubbly flow, the pressure gradient will be responsible for transverse migration of the bubbles towards the center of the pipe. If the rotation is overestimated, so will be the migration of bubbles which results in an excessive bubble accumulation in the core of the flow that should induce an overestimation of the local void fraction. This qualitative behavior is in agreement with the too large void fraction obtained in the simulations of DEBORA-Promoteur Te69 cases (Figure 11.2).

Moreover, the discrepancy on the rotation increasing with the distance to the mixing vanes implies that boiling simulations would be more accurate for the C5200 cases than the C4800 cases (measurements 10  $D_h$  downstream the MV versus. 23.5  $D_h$ ). That is actually true when looking at the void fraction profiles for Te65 and Te69 cases (Figures 11.2a and 11.2b) where larger differences with the measurements are observed for the C4800 simulations.

**Remark :** The main limitation of the presented single-phase simulations is the systematic use of a wall-law, which can have a strong impact regarding this geometry where the wall presence is ubiquitous in addition to the mixing vanes presence. A LES computation using an even finer meshing allowing to reach  $y^+ \sim 1$  in the computational domain could bring insightful information to investigate the rotation overestimation.

### 11.3 REGARDING CHF DETECTION IN MIXING VANES GEOMETRY

As a perspective test, we want to visualize the evolution of the CHF criterion of Zhang [174] (value of the CHF triplet  $N_{sit,a} \pi \langle R \rangle^2 t_{gf}$ ), as in Section 9.3 on a DEBORA case, for a geometry including mixing vanes. To do so, a simulation of a boiling upward flow in a  $5 \times 5$  heated rod bundle is conducted. The geometry includes two PWR mixing grids and a non-uniform heating is applied with the 9 central rods having a larger wall heat flux. The initial NEPTUNE\_CFD Heat Flux Partitioning is used (Section 2.5) to compute the CHF triplet value.

**Note :** As in Section 9.3, the values of the CHF triplet attained in the computation are not in the range of [0,1] as it should be prior to CHF [174] since the closure laws for boiling parameters are not precise enough.

On Figures 11.10 and 11.11 we present values obtained for the CHF triplet on the rods respectively at the first and the second grid. Wall areas where the CHF triplet is high are the zones closer to the boiling crisis.

At the inlet upwards the first mixing vane (Figure 11.10), the CHF triplet gradually increases similar to a simple tube case (Figure 9.7) with the central rods exposed to a larger heat flux reaching greater values of the CHF triplet. After the vanes, the local values of the CHF criterion are significantly diminished both for peripheral and central rods, with non-symmetric patterns related to the rotating flow induced by the mixing vanes.

When reaching the second grid (Figure 11.11), the difference in CHF triplet values between central and peripheral rods is less important which is probably an effect of the upwards mixing of the first grid. After the second grid, the CHF triplet values are also globally reduced similar to what was observed at the first grid (Figure 11.10). The CHF triplet is though larger when reaching the second grid, which is logical since the fluid is continuously heated between the two grids. Higher risk of boiling crisis would seem to be right upstream the second grid.

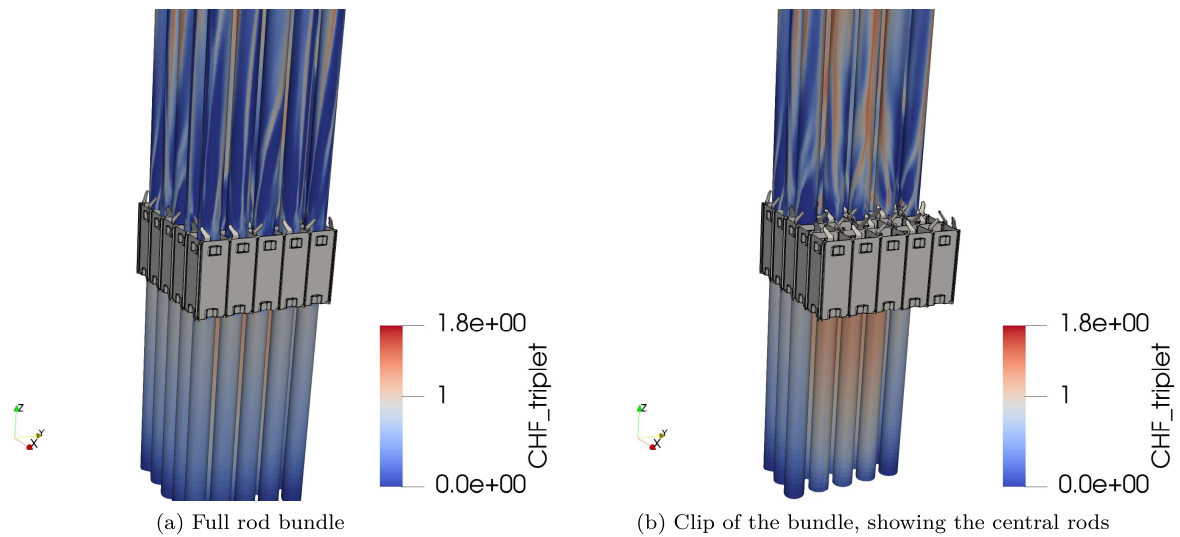


Figure 11.10: Visualization of the CHF triplet value around the first grid. (Computation results courtesy of Vladimir Duffal)

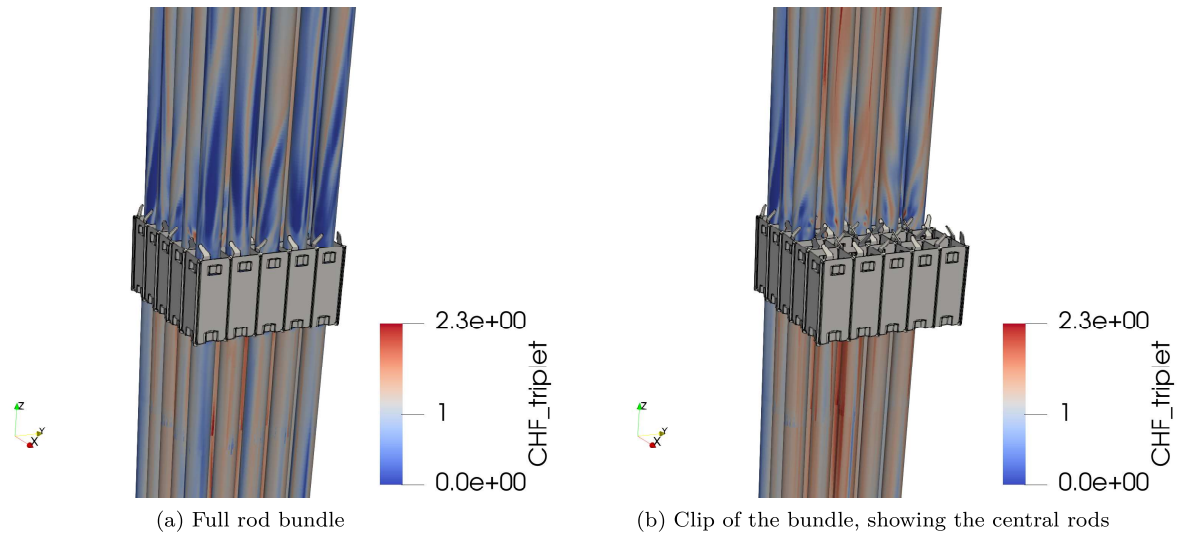


Figure 11.11: Visualization of the CHF triplet value around the second grid. (Computation results courtesy of Vladimir Duffal)

Altogether, those observations, though purely qualitative, are presenting interestingly coherent features regarding boiling crisis occurrence for PWR with overheated rods have larger CHF triplet values and mixing grids actually decrease the CHF triplet thanks to their mixing effect.

## 11.4 CONCLUSIONS

In this Chapter, we performed CFD simulations on the tube equipped with mixing vanes geometry. Both boiling flow simulations using NEPTUNE\_CFD and single-phase simulations with *code\_saturne* were realized, respectively compared to DEBORA-Promoteur and AGATE-Promoteur experiments. So far, the main highlights of the results are:

- The boiling simulations of DEBORA-Promoteur cases showed reasonable qualitative behavior with bulk vapor accumulation, void fraction peak and bubble coalescence at the center, and vapor velocity increase with outlet quality.
- Yet, precise predictions of void fraction profiles could not be achieved with very large overestimation in the bulk plus the incapacity to reach void fractions higher than 70%. This could be associated to change in the multiphase flow regime that lie outside of the dispersed bubbly flow model capacity.
- Further investigations on the single phase case AGATE-Promoteur showed an excessive computed rotation of the fluid, increasingly differing from the experiments as we move downstream the mixing vanes. A too large swirl could explain the overestimation of the void fraction in the boiling case due to bubble transverse migration.
- Wall law seems to have a significant influence over the velocity profiles and may be an area of improvement, especially for confined geometries where solid walls are strongly influencing the flow.

**Remark :** We want to mention that achieving precise results for single-phase simulations on complex industrial geometries representative of PWR is still a very active field of research [94]. The use of RANS [7] or wall-modeled LES [53] approaches are still investigated in order to save computational time in the prospect of reaching simulations of a full fuel assembly by including, for instance, modeling of mixing vanes as source terms in the computational domain [20].

- Evaluating values of the CHF triplet as a qualitative indicator of boiling crisis risk of occurrence (Section 9.3) on a rod bundle including mixing vanes showed presented a good perspective with physically coherent evolution regarding the overheated rods and mixing grids effects. This could be compared to boiling crisis location in experiments to further validate its behavior.